The Academic
International Journal of Multidisciplinary Research

An Online Peer Reviewed / Refereed Journal
Volume 4 | Issue 10 | October 2026
ISSN: 2583-973X (Online), SJIF IF(2026): 5.6
Website: www.theacademic.in

A New Electrochemical Sensor Platform for the Sensitive Determination of Nitrofuran Derivative Furazolidone in Biological Samples

Palpandi Karuppaiah

*Corresponding author Email:sensorpandian18@gmail.com, ORCID ID: 0009-0003-2698-3455

DOI : https://doi.org/10.5281/zenodo.24492808

ARTICLE DETAILS

Research Paper

Received: 01-11-2026

Accepted: 08-11-2026

Published: 20-11-2026

Keywords:

functionalized multi-walled carbon nanotubes, chemical oxidation, electrocastalysis, amperometric, disposable electrode, specific capacitance, biomedical application, occupational health and safety.

ABSTRACT

Furazolidone (FUR), an organic chemical used largely as a veterinary medicine to treat bacterial infections in cattle, may endanger consumer health, if found in food items. As a result, there is an urgent need for a trustworthy and fast way of detecting FUR to assure food safety. In response, electrochemical sensors have received a lot of attention due to their numerous benefits, including high sensitivity, ease of operation, quick analysis, and user-friendliness. This comprehensive study, motivated by the imperatives of food safety and pharmaceutical quality control, seeks to capture recent advances and strategies in the development of diverse electrocatalysts tailored to specific criteria such as sensitivity, selectivity, and intended applications for FUR detection. The present work carefully examines a new electrocatalyst modified electrodes intended for electrochemical detection of FUR in biological samples.

1. Introduction

A nitrofuran derivative with anti-bacterial and anti-protozoal qualities is furazolidone, also known as furaxone. By attaching itself to bacterial DNA, furazolidone progressively inhibits monoamine oxidase. It is frequently applied to the treatment of infectious diarrhea. It is believed that furazolidone and the free radicals it produces bind DNA and create crosslinks. This drug has a strong effect on bacterial DNA, which

Disclaimer: The opinions, interpretations, conclusions, recommendations, analyses, and statements expressed in this research article are solely those of the author(s) and do not reflect the views, policies, or positions of the Publisher, Chief Editor, Editors, Editorial Board, Reviewers, or their affiliated institutions. The author(s) are solely responsible for ensuring the originality, authenticity, and integrity of the manuscript and for ensuring that it is free from plagiarism, AI-generated content, copyright infringement, data falsification, and any other form of academic misconduct.

leads to a large number of mutations (transitions and trans versions) in the bacterial chromosome. Nitro-reduction to the amino furan derivative has been shown to be the primary metabolic pathway for furazolidone, which is metabolized quickly and extensively. Beta-hydroxyethyl hydrazine (HEH) and 3-amino-2-oxazolidone (AOZ) are the two primary metabolites that are generated. Monoamine oxidase inhibition is caused by AOZ. The main process for drug excretion and detoxification is conjugation with glutathione.

Furoxone possesses an extensive antibacterial spectrum that encompasses most gastrointestinal tract pathogens, including E.coli, staphylococci, Salmonella, Shigella, Proteus, Aerobacter aero genes, Vibrio cholera, and Giardia lamblia. Its bactericidal effect stems from its interference with DNA replication and protein creation; this antimicrobial action reduces the emergence of resistant organisms. Furazolidone and its free radical products are thought to bind DNA and cause cross-linking. Bacterial DNA is extremely sensitive to this medication, resulting in a significant number of mutations (transitions and trans versions) in the bacterial chromosome [1]. Side effects of furoxone include low blood pressure, urticaria, fever, arthralgia, and a vesicular morbilliform rash. Other negative effects include dark urine and hemolysis in G6PDH deficient persons. The medication inhibits monoamine oxidase (MAO) and should not be provided concurrently to anyone who is already on MAO inhibitors. [2-9].

Various detection methods, including HPLC, mass spectrometry, and spectrophotometry, have been developed to identify these compounds. However, while these approaches work effectively, they are constrained by their high cost and complex operation. Developing electrochemical sensors for DA, UA, and FUR is crucial, because of their mobility and simplicity [10]. As a result, the demand for speedy and easy FUR monitoring in actual samples has increased significantly, and establishing a particular and sensitive analytical approach is vital to identify FUR reliably for food safety and ecological pollution monitoring. Herein, we developed the new sensing platform for the sensitive determination of Furazolidone in biological samples using functionalized multi-walled carbon nanotubes modified scaffold and it is capable for real-time practical applications.

Since their discovery, carbon-based nanomaterials, particularly Multi-Walled Carbon Nanotubes (MWCNTs), have gained a great deal of attention due to their distinct electrical, optical, physical, chemical, and mechanical capabilities. Multi-walled carbon nanotube synthesis, purification, structural characterization, functionalization, and application have all seen remarkable advancements. For Their specific characteristics make them well-suited for a plethora of application areas, namely nanoelectronic, energy management, electrocastalysis, materials science, the construction of biosensors based on different

detection schemes, multifunctional Nano probes for biomedical imaging, sorbents for sample preparation or removal of contaminants from wastewater, as anti-bacterial agents, drug delivery Nano carriers, etc., current relevant application areas are counted [11-15]. MWCNTs offer several capabilities to electrochemical sensors, making them ideal for analytical reasons. Electrochemical interactions between analytes and electrodes can generate important analytical signals. These interactions can be either electrically induced or spontaneous at zero current. Electrochemical sensors may be classified into four types: voltammetric, potentiometric, solid electrolyte gas sensors, and chemically sensitized field effect transistors. MWCNT's enormous surface area (~1600 m^2g^{-1}) and outstanding electrical conductivity (current densities up to 109 Amp cm^{-2}) make them ideal for downsizing and portability in systems [14]. Present days, Electrochemical MWCNTs-based sensors are widely used in several fields, including medicine, clinical diagnostics, pharmacology, food industry, sanitation, occupational safety, forensic chemistry, and environmental analysis [16-22].

Multi-Walled Carbon Nanotubes (MWCNTs) may be produced utilizing a variety of intriguing processes, each with distinct advantages based on the desired purity, scalability, and structural features. Here's a breakdown of the most popular methods: such as Chemical Vapor Deposition (CVD) [23], Arc discharge method [24-25], Laser ablation method [26], hydrothermal method [27], Electrolysis method [28], Solar technique [29], Chemical Synthesis [30]. Several carbon nanotube based electrodes have been developed for the electrochemical sensor platform, including MWCNT-based electrochemical sensors offer significant benefits for analytical applications, including increased detection sensitivity, low charge-transfer resistance (Rtc), electrocatalytic effect, and decreased fouling. It is also thought that residues of metallic catalysts might add significant. The electroanalytical properties of nanotubes have a beneficial synergistic impact, facilitating gadget development [44].

2. Experimental

2.1. Materials and reagents

All the chemical substances are of analytical grades were utilized without any further purification. Neat multi-walled carbon nanotube is been received from Merck chemicals. Nitric acid, sulphuric acid, dimetrozolidone, carbamacibine, dopamine, hydrogen peroxide, citric acid, vitamin-C, glucose, paracetamol, lead, cadmium, arsenic, sulphate, chloride, monobasic sodium phosphate and disodium hydrogen phosphate were obtained from Merck chemicals. The supporting electrolyte solution (0.05M PBS, pH-7.0) was prepared by the mixture of mono and dibasic sodium phosphates with doubly distilled water.

2.2 Instrumentation and methods

The electrocatalytic analysis was carried out at the CHI-1211 work station. Electrochemical investigations are analyzed using a typical three-electrode setup. Screen printed carbon electrodes (SPCE) serve as working electrodes, saturated potassium chloride (KCl) Ag/AgCl as reference electrodes, and platinum wires as counter electrodes. X-ray powder diffraction (XRD) was performed using an XPERT-PRO diffractometer equipped with a Cu Kα ratio of k=1.54Å. To determine the surface morphological characteristics of the prepared samples, observations are made using a field emission-scanning electron microscope (FE-SEM) of HITACHI S-3000H equipped with an energy dispersive X-ray spectrometer and an accelerating voltage of 20kV, as well as High Resolution Transmission Electron microscopy (HR-TEM) of TECNAI with an equivalent accelerating voltage of 200kV. For spectral data processing, the Nicolet 410-FT/IR spectrophotometer's Fourier transform infrared (FT-IR) was employed.

2.3 Preparation of functionalized multi-walled carbon nanotubes (*f*-MWCNTs)

Impurities were removed from pure MWCNTs using 35% hydrochloric acid. In a 500 mL round-bottom flask, 1 g of MWCNTs were introduced, followed by 200 mL of 35% HCL. The mixture was agitated with a magnetic stirrer for 1 hour (2500 rpm), then diluted in 1 liter of water, filtered, rinsed five times with deionized water, and filtered through membrane filter paper (0.002 micron) attached to a vacuum pump. The product is then allowed to dry overnight in a lyophilized at 55°C to eliminate any contaminants and excess moisture content. To further oxidize the purified MWCNTs, about 1.0gm of the purified MWCNTs were distributed in 300 mL of 16 mole nitric acid (95%) in a 1000 mL round bottom flask and 16 mole sulphuric acid (300 mL) in a 1:1 ratio, fitted with a condenser. The dispersion was held at 98°C for 2 hours, stirring constantly. The resultant dispersion was neutralized in water (pH 7.0), filtered, and dried in a vacuum at 55°C overnight. The modified CNTs (*f*-MWCNTS). Moreover, the synthesis mechanism of *f*-MWCNT is elabotared in **Scheme 1**.

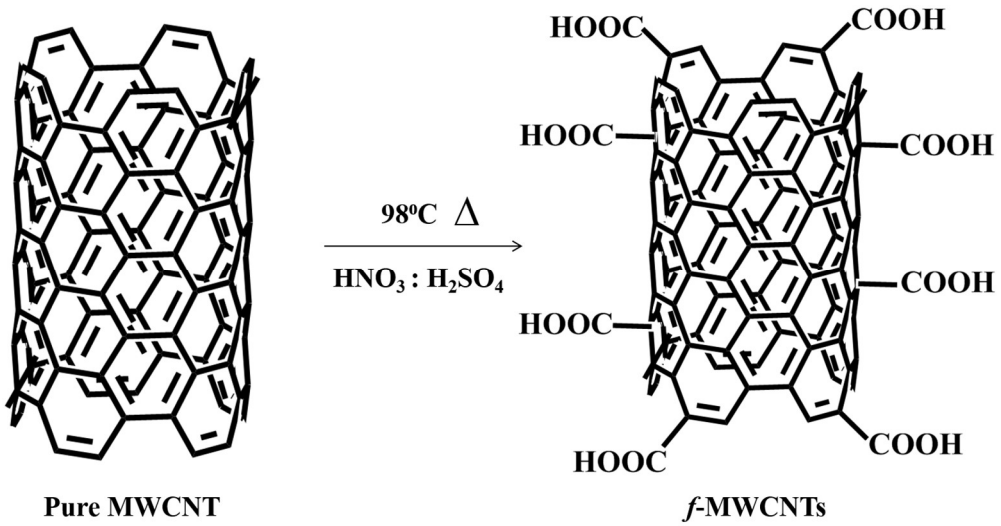

Scheme 1. Synthesis of *f*-MWCNTs.

2.3 Fabrication of *f*-MWCNTs on SPC electrode

The as-prepared *f*-MWCNTs (0.05g/mL^{-1}) was dispersed in DMF and it is sonicated for 60 minutes to form a homogeneous colloidal suspension. The electrode fabrication process was carried out by approximately 2µL of *f*-MWCNTs drop casting on the naked surface of SPC electrode and is dried at 70°C in hot air oven for 5 mints. Thus the developed electrode denoted as *f*-MWCNTs/SPCE. It is used for further electrochemical investigation. The schematic diagram **2** illustrates the fabrication of the electrode.

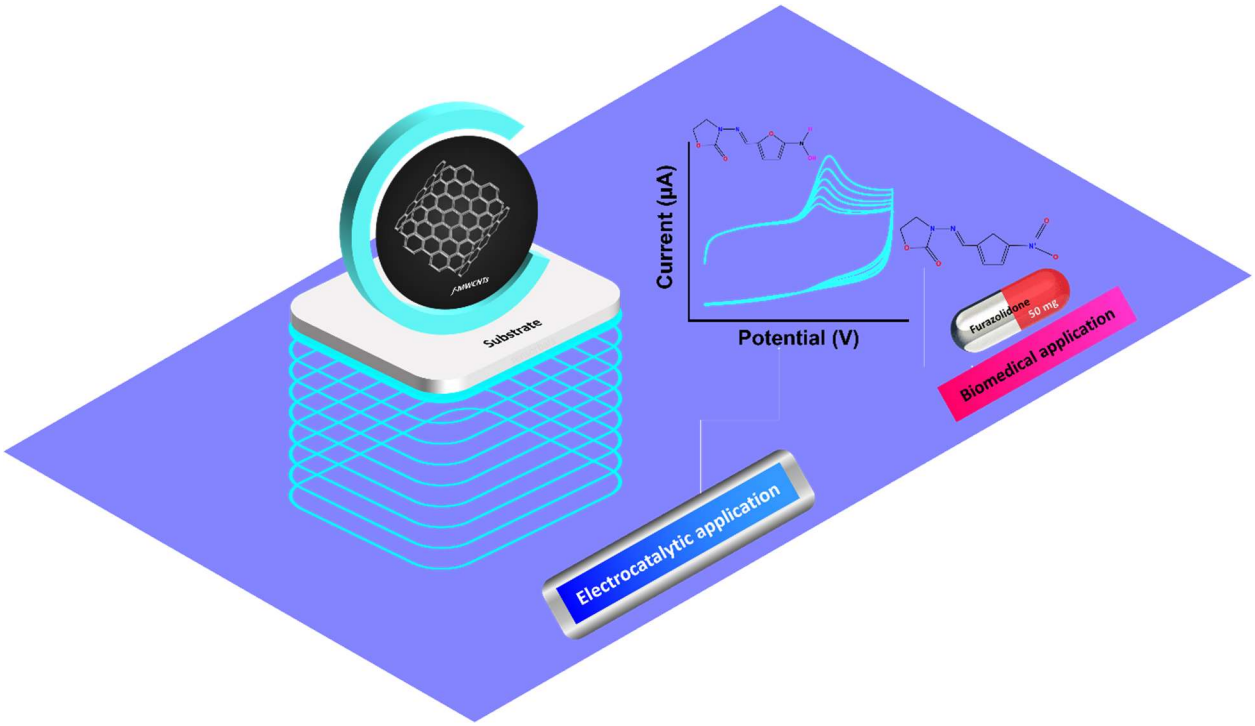

Scheme. 2 Fabrication of *f*-MWCTs on Screen-printed carbon Electrode.

2.4 Preparation of stock solution

In order to demonstrate the practical applicability of the proposed sensor (FUR) were quantified in Human urine (HU), human serum and artificial saliva on *f*-MWCNTs/SPCE. This sample was prepared before the experiment and three parallel determinations were carried out for this biological sample quantification. Consequently, the results obtained demonstrate the practical applications of the constructed sensor in actual samples.

3. Results and Discussion

3.1. Selection of MWCNTs

Many other types of electrochemical research have been proposed using carbon nanomaterials, such as carbon nanotubes. In this study, we chose multi-walled carbon nanotubes for sensor application due to its better sensitivity, faster response time, low-cost, large-volume of manufacturing, low-resistance, high electrical conductivity, dispersability, and ease of sensor construction. In general, carbon sources are environmentally beneficial and readily available. Carbon nanotubes, in particular, have extraordinary electrochemical properties.

3.2 Quality control and morphological analysis

The observed surface morphological properties of as prepared multi walled carbon nanotubes were confirmed by field emission scanning electron microscopy (FE-SEM) and high resolution transmission electron microscopic technique. The FE-SEM morphographs of *f*-MWCNTs were given in **Fig. 1 A** which illustrates *f*-MWCNTs formation under the optimized reaction condition and the corresponding particle size distribution histogram data shown in **Fig.1 B**. from the FE-SEM database we are calculated the average particle size of the as-prepared *f*-MWCNTs is (D=28.33 nm) associated with the standard deviation σ_D is 1368 nm respectively.

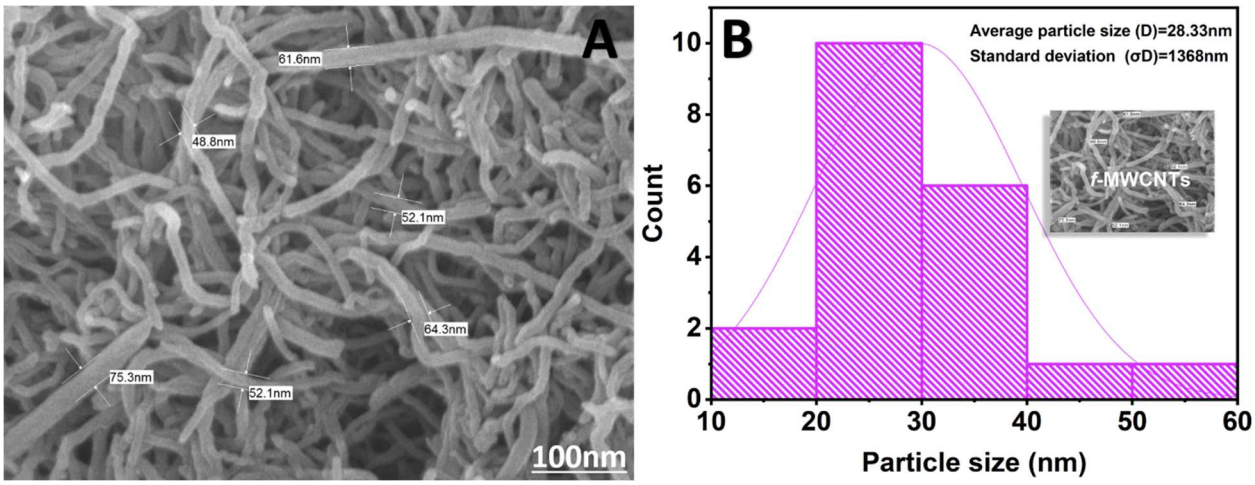

Fig. 1 (A). FE-SEM photograph and average particle size of *f*-MWCNTs (**B**).

To analyze the morphological features of as-prepared *f*-MWCNTs were conducted in high resolution transmission electron micrograph (HR-TEM) as shown in **Fig 2 A** which exhibits the estimated average particle size of the carbon nanotubes is 69.94 nm, along with the standard deviation is 1.613 nm, which are estimate from the fitting of particle size distribution histogram using long-normal distribution function. The histogram data is illustrated in the **Fig 2 B**, also the long-normal distribution function, which is interpreted as the equation (1),

$$f\ (D) = \left(\frac{1}{\sqrt{2\pi}\sigma_D}\right)^{\cdot} \exp - ln^2\ \left(\frac{D}{D_0}\right)\ /2\sigma^2 \rightarrow (1)$$

Here, D correspond to the average particle size and σ_D is the standard deviation.

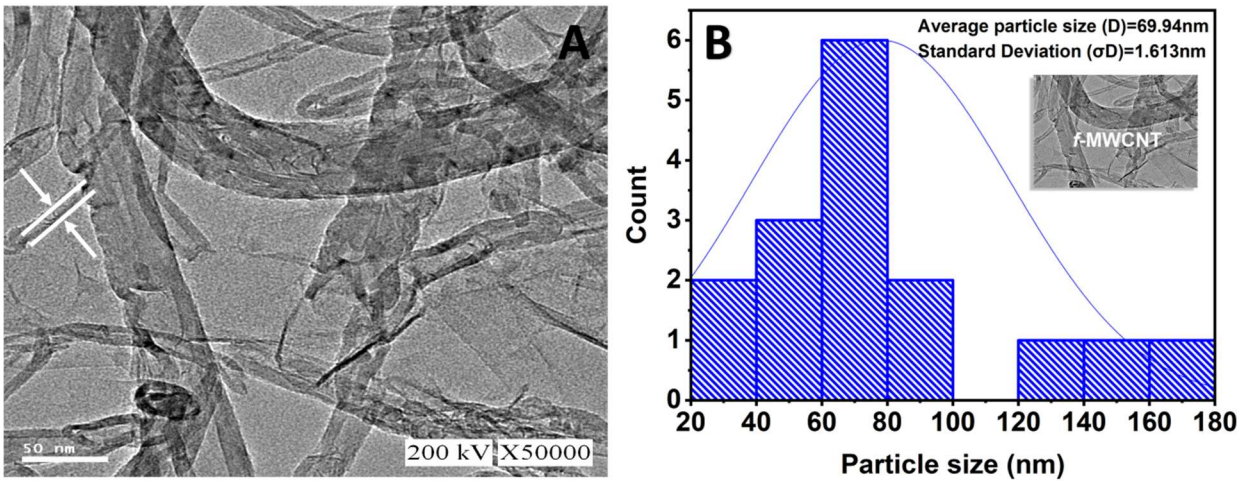

Fig. 2 (A). HR-TEM morphographs of *f*-MWCNTs fitted with

long normal distribution function (**B**).

Simultaneously, an energy dispersive X-ray analysis (EDS) analysis was used to evaluate the *f*-MWCNTs, materials purity, the determination of elemental composition consisting within the materials after functionalization process, as depicted in **Fig 3 A.** From the EDS spectrum, the presence of carbon and oxygen elements in the *f*-MWCNTs, were confirmed. These data indicated that the nanomaterials are well oxidized in the given reaction time and the acidic (-COOH), basic functional groups (-OH) significantly formed. The weight percentages of C and O in the *f*-MWCNTs, calculated using EDS results were 22.3% (Oxygen) and 77.7.0% (Carbon) respectively (Statistical data for elementals present in the *f*-MWCNTs illustrated in **Table 1** associated with mapping images **Fig 3 B**).

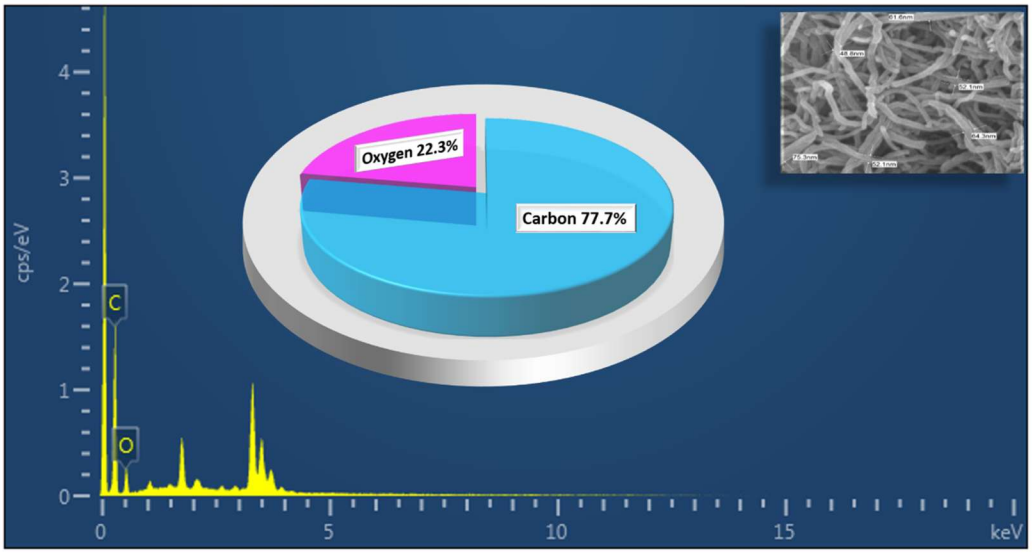

Fig. 3 (A) Energy dispersive X-ray spectrograph of *f*-MWCNTs.

Elements	At%	Wt%
Carbon	77.7	1.11
Oxygen	22.3	1.11
Total	100	100

Table 1. Elemental composition data for *f*-MWCNTs.

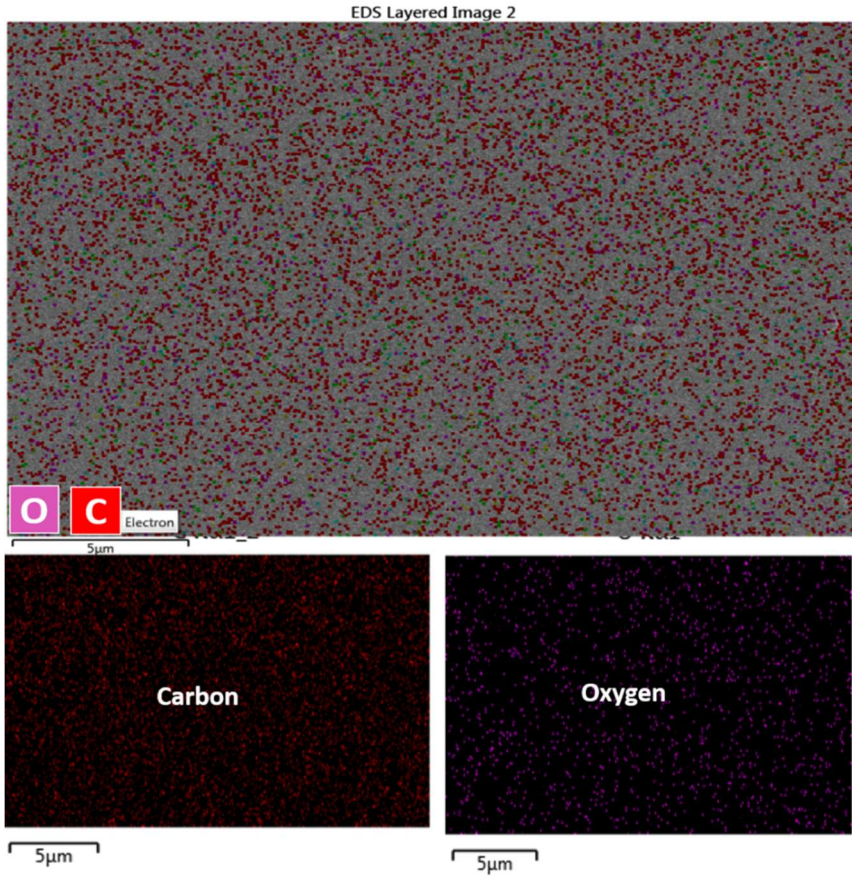

Fig 3 (B). Elemental mapping of *f*-MWCNTs.

The crystalline nature of *f*-MWCNTs, was investigated by XRD technique and the corresponding XRD patterns were revealed in **Fig 4**. XRD spectrograph of the as-prepared *f*-MWCNTs exhibited well-defined sharp peak at 25.92 and the smaller peak also observed at 43.07 2theta degrees were assigned to the corresponding planes 002 and 100 respectively. Additionally, a characteristic diffraction peak in the form of *f*-MWCNTs was grasped at 25.92°(2θ) demonstrating the crystal plane (002) of *f*-MWCNTs which represents the plane reflection of the carbon materials. There are no other characteristic peaks of impurities or precursors were observed, thus indicating the formation of a pure phase *f*-MWCNTs. The average crystalline of *f*-MWCNTs was examined using the full-width half maximum (FWHM) value of prominent diffraction peak of the XRD pattern through Scherer's equation (2) as follows [42],

$$X_s = k\lambda|\beta\cos\theta \ \rightarrow \ (2)$$

Where Xs represents the crystal size, λ denotes the wavelength of the X-ray, ß signifies the full width at half maximum (FWHM) of the diffraction peak (observed value β = 0.54832), and θ is the diffraction angle, and k is Scherer's constant. The crystal size was calculated from the diffraction plane (002), and the average

crystalline size of the *f*-MWCNTs, was found to be 26.9806 nm with the calculated lattice micro strain (ϵ) is 0.00598 and the formula is described in equation (3) Lattice micro strain formula;

$$\text{Lattice micro strain } (\epsilon) = \frac{F.W.H.M}{(4\ X\ tan\theta)} \quad \rightarrow \quad (3)$$

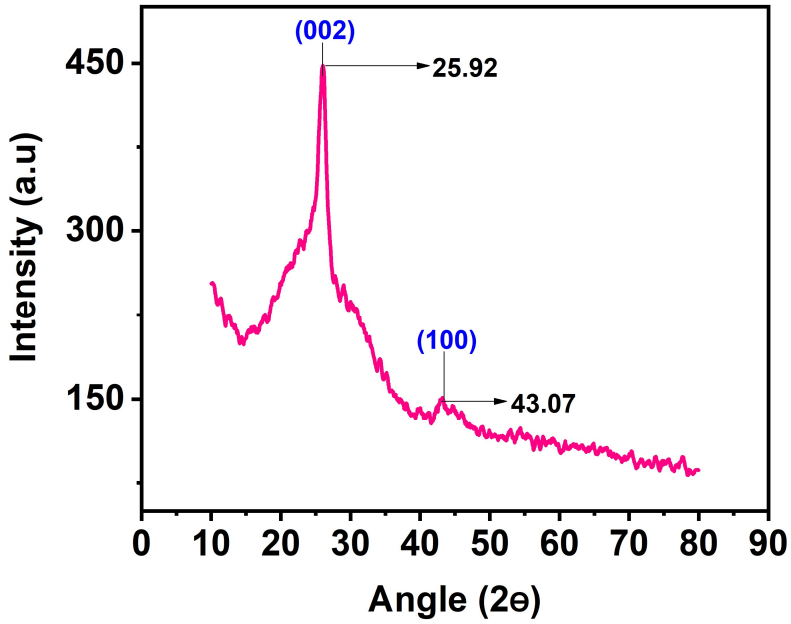

Fig 4. X-ray diffraction spectra of *f*-MWCNTs.

Moreover the obtained d-spacing values of as synthesized *f*-MWCNTs were confirmed by Braggs' Law and it is elaborated .To calculate the d-spacing of *f*-MWCNTs from the XRD peaks value such as 2Θ = 25.92 and 2Θ = 43.07 respectively, (eqn 4)

$$n\lambda = 2d\sin\Theta \quad \rightarrow \quad (4)$$

Where;

n is the order of reflection (usually 1)

λ is the X-ray wavelength (for Cu Ka, it's typically 1.5418 Å)

Θ is the angle of incidence (half of the 2Θ value (FWHM))

D is the interplanar spacing.

$\theta = \frac{25.92}{2} = 12.96^0$ (sin (12.96^0) ~0.22427).

Using Cu Ka radiation: λ = 1.5418 Å

$$d = \frac{n\lambda}{2sin\theta} = \frac{1.5418}{2\sin(12.96^0)} \sim \frac{1.5418}{2.0.2243}$$

D = ~ 3.44 Å for 2Θ = 25.92^0

As well as we gain the d spacing value for 2Θ = 43.07^0 is ~ 2.10 Å. (sin (21.535^0) ~0.3666).

Fourier transform infrared spectroscopy (FT-IR) was utilized to investigate the chemical and structural properties of the produced *f*-MWCNTs, as well as the influence of the chemicals employed. **Figure 5** illustrates the IR spectra for *f*-MWCNTs in the 400-4500 cm^{-1} range. **Figure 5** depicts the FT-IR results for functionalized MWCNTs treated with HNO_3/H_2SO_4 (3:1) in the range 600 to 4600 cm^{-1}. The FT-IR spectra from the carboxylic stretching frequency in *f*-MWCNT occurred at 1699.04 cm^{-1}, showing that carboxylic groups are produced as a result of the oxidation of certain carbon atoms on the surfaces of the MWNTs by the HNO_3/H_2SO_4 combination. The stretching vibration (O-H) was observed at 3013.311 cm^{-1}, 3672.02 cm^{-1}, and 3858.75 cm^{-1} in the MWCNT-COOH, as shown in **Fig. 5**, and can be assigned to the O-H stretch from carboxyl groups (O=C-O-H and C-OH), whereas the peak at 2898.95 cm^{-1} can be associated with asymmetric and symmetric C-H stretching. The peak at 1699.60 cm^{-1} can be associated with the stretching of the carbon nanotube backbone. The signal at 1163 cm^{-1} might be attributed to C-O stretching in the same functionalities, but the peak at 1387.14 cm^{-1} in functionalized MWCNTs corresponds to the carboxylic acid group's O-H bending deformation mode. In **Fig. 5**, the wide absorption band at 3672.02 cm^{-1} is due to the O-H stretch of the hydroxyl group, which may be attributed to the oscillation of carboxyl groups (O=C-OH and C-OH). Carboxyl groups on MWCNT surfaces may be produced by surface oxidation during acid mixture treatment.

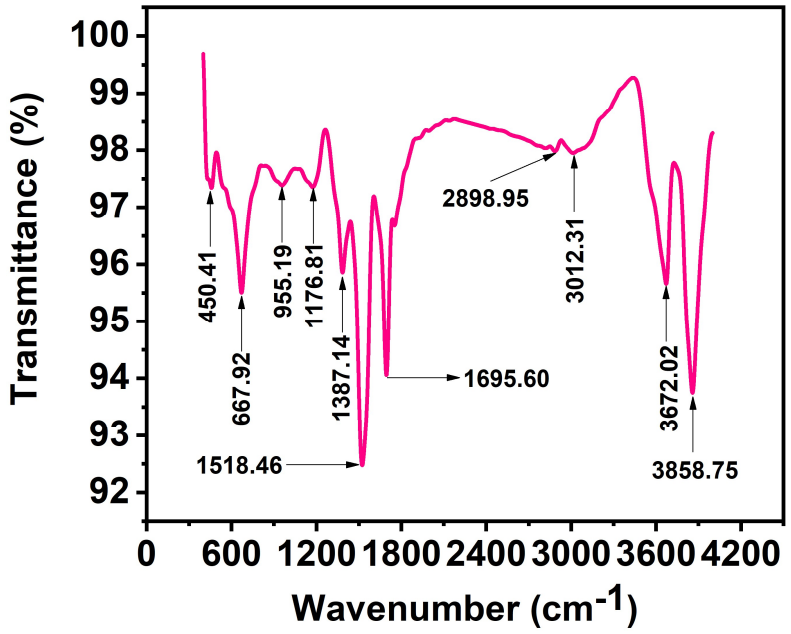

Fig 5. FT-IR spectral data for *f*-MWCNTs.

Raman spectroscopy is the most important tool for CNTs, providing information like as doping, defects, chirality, curvature, and diameter analysis. Raman tests were performed in this study using a green excitation laser with a wavelength of 668. **Figure 6** depicts the spectra of MWCNTs functionalized with HNO_3/H_2SO_4. MWCNTs' Raman spectra typically have two peaks: D and G bands. The D band at ~1351 cm^{-1} in MWCNT samples reveals scattering from low defects and amorphous carbon. It's a disorder-induced peak. Carbon nanotubes without defects exhibit an organized high-frequency in-plane stretching of C-C bonds, resulting in the G band peak (~1587 cm^{-1}). It's called a graphite band. This band may be observed in defect-free Sp^2 carbons without the need for an elastic defect-related scattering mechanism. The ratio of the intensities of the D and G bands (I_D/I_G) is related to the amount of defect development, hence it may be used to assess oxidation. As shown in **Figure 6**, the ratios for functionalized MWCNT oxidized with HNO_3/H_2SO_4 are 0.85. An rise in the I_D/I_G ratio implies that MWCNT sidewalls have no flaws.

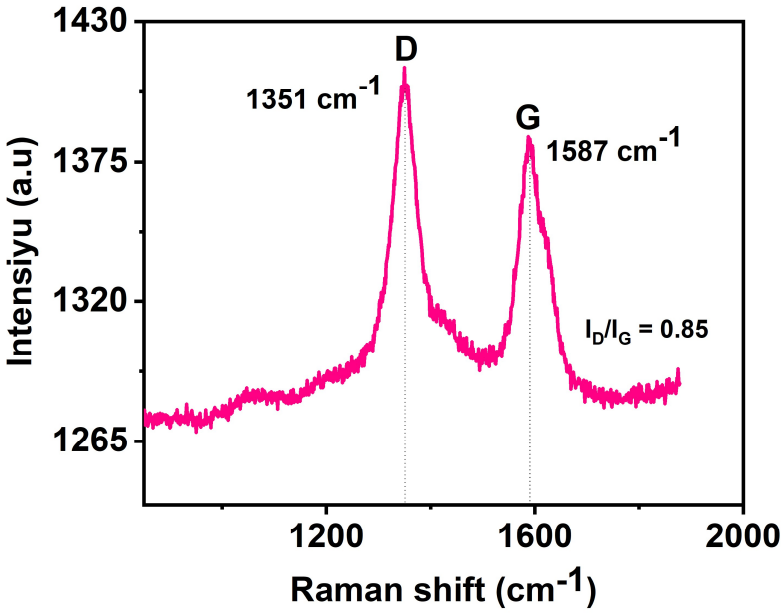

Fig 6. Raman spectroscope of *f*-MWCNTs.

3.3 Electrochemical analysis

A three-electrode standard electrochemical station was used in potentiostatic conditions (CHI 112, USA). A saturated KCl-Ag/AgCl was employed as a reference electrode, while platinum wire (Pt) served as a counter electrode. The functioning electrode was created by fabricating *f*-MWCNTs on a bare screen printed carbon electrode. At various scan speeds, the cyclic voltammetry method was used in a potential window ranging from -0.2 to 0.6 V, beginning with an open circuit potential. PBS (0.05M) adjusted to pH 7.0 is employed as a supporting electrolyte. Phosphate buffer solution (0.05M) used as the supporting electrolyte adjusted to pH 7.0. The solutions were purged with nitrogen gas for 20 minutes before to use. The capacitance $C = i_{dt}/d_E$ was determined as 0.0006666 using the current versus potential characteristics acquired at different scan speeds. For the *f*-MWCNTs/SPCE-modified system, all studies were conducted at room temperature and at 25°C. All compounds were used exactly as supplied, with no additional purification.

3.4 Specific capacitance of the electrode (*f*-MWCNTs/SPCE)

Additionally, the typical CV curves of the *f*-MWCNTs/SPCE based electrodes in the 1M KOH electrolyte at the scan rates (10mV/s) are shown in **Fig 7**. The curve displayed quasi-isosceles shape with redox peaks, indicating an ideal capacitive behavior, specific capacitance and also the cyclic voltammetry curve demonstrating an excellent capacitor behavior of the modified electrode.

The specific capacitances (SC) were calculated using the following equation (5):

Charge (Q) = Integrated area/2*scan rate (~10 mV/s)

$$SC = I^*\Delta t/(\Delta V^*m) \rightarrow (5)$$

where I (A) is the discharge current, m (g) is the mass of the drop casted material on the electrode surface, and ΔV (V) is the potential change within the discharge time (scan rate) Δt (s). the obtained specific capacitance (SC) of the electrode is 133.3 F/g.

Along with, using the koutecky-levich (K-L) equation surface covering of FUR electroactive species is been calculated as follow the equation (5);

$$\Gamma = Q/nFA \quad \rightarrow \quad (5)$$

In equation (1), Q represents charge reduction and Γ represents surface area (mol cm^{-2}). Where n is the total number of electron transfers in the reduction process, and A is the electrode's surface area. F stands for the faraday constant (96485.33289(59) C mol^{-1}). The overall surface coverage of *f*-MWCNTs/SPCE FUR is determined to be around 6.7539 mol cm^{-2}. With such a huge covering surface area, FUR can readily boost its adsorption ability towards *f*-MWCNTs/SPCE, resulting in a strong current response during the FUR reduction process.

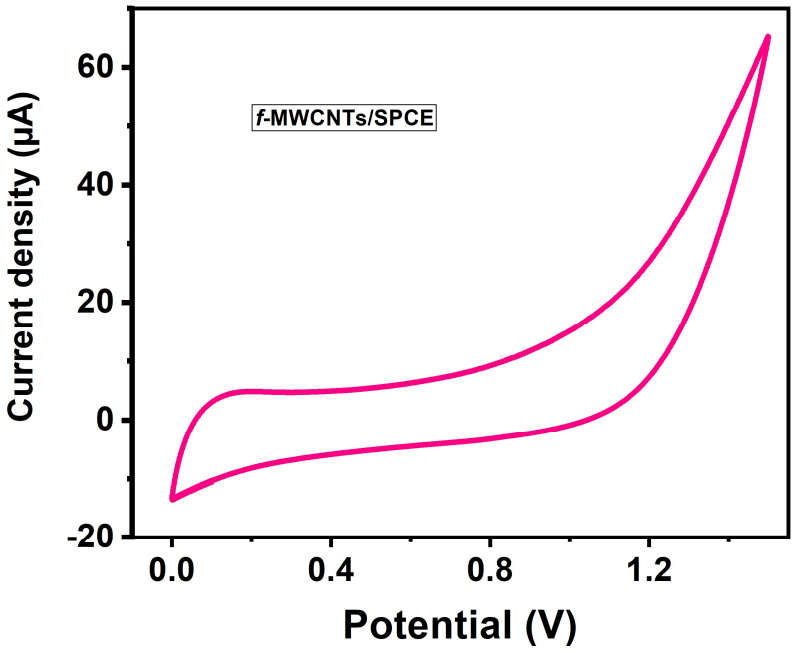

Fig 7. Specific capacitance of the *f*-MWCNT$_S$ CV data.

3.5 Electroanalytical characteristics of *f*-MWCNTs/SPCE on the analyte (Furazolidone)

The electroanalytical performance of *f*-MWCNTs/SPCE is been studied using nitrogen saturated atmosphere within the pH-7.0 Phosphate buffer solution (PBS). Here the cyclic voltammetry (CV) runs were analyzed with a 100 µM of Furazolidone in a fixed scan rate of 0.05 mV/s^{-1}. **Fig. 8 A** shows the comparison studies of bare and *f*-MWCNTs/SPC electrode which encloses bare (dotted blue), *f*-MWCNTs/SPCE (brown). Bare SPCE reveals a poor electrocatalytic activity with an significant reductive peak current of (I_{pc}=-0.3770 V). Curiously a high reduction peak is been observed for *f*-MWCNTs/SPCE (I_{pc}=-0.3786 V) with comparison to bare electrode and the peak current chart illustrated in **Fig 8 B.** When *f*-MWCNTs/SPCE is used as a modifier on the SPCE surface with a high reduction peak current a curve is been directed with a shifting peak potential onwards of the least reduction potential this is due to the irreversible direct electrochemical reduction of nitro groups -R-NO_2 into hydroxylamine-R-NHOH. The possible reduction mechanism of FUR on *f*-MWCNTs/SPCE is illustrated in the **Scheme 3**.

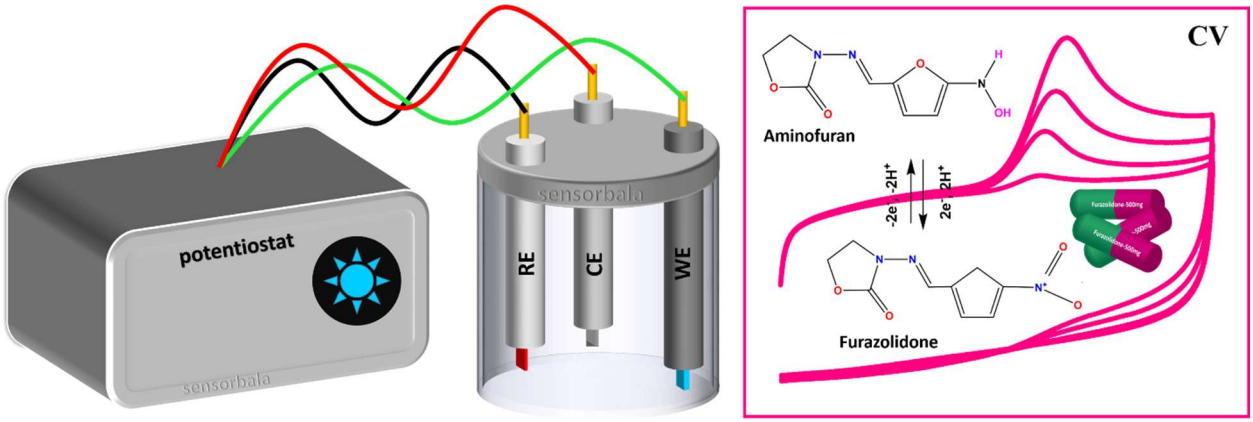

Scheme 3. Electro-reduction mechanism of an analyte on the modified electrode.

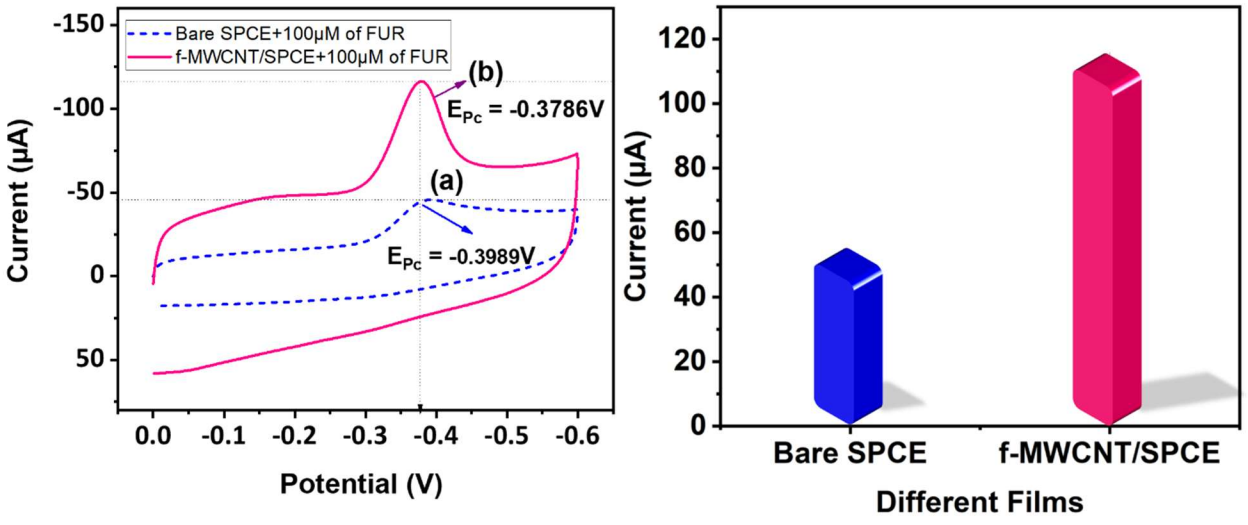

Fig 8 (A) . CV data visualization for different films respect with the current response **(B).**

The quantification of FUR on *f*-MWCNTs/SPCE modified electrode provided the 3.85 fold higher peak current response, when compared to unmodified electrode (bare SPCE). This behavior can be compared with the π-π stacking as the enhancement of the electrocatalytic activity and electrostatic interaction among *f*-MWCNTs/SPCE and FUR. Continuing, the heterogeneous electron transfer rate of *f*-MWCNTs/SPCE and also the larger active surface area has clearly simplified in determination of FUR. The overall reduction mechanism of the furazolidone were elaborated in **Fig 8 C.**

Step-1

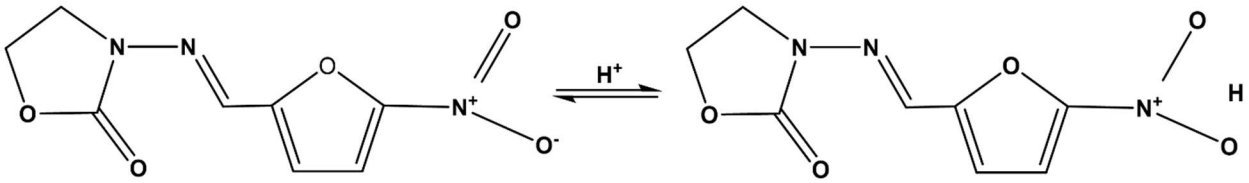

Furazolidone ($-NO_2$) **Furazolidone intermediate**

Step-2

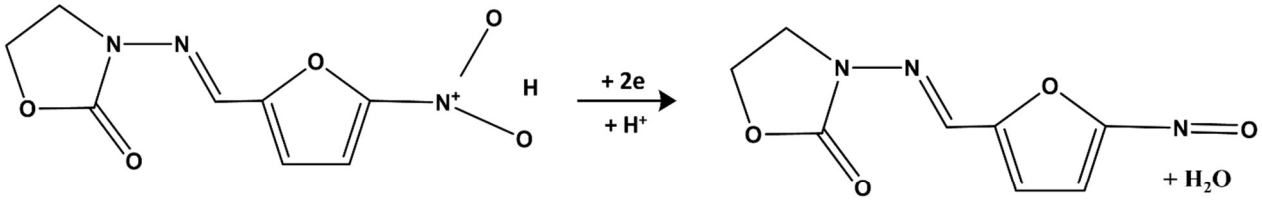

Furazolidone intermediate

(*E*)-3-(((5-nitrosofuran-2-yl)methylene)amino)oxazolidin-2-one

Furazolidone (-NO)

Step-3

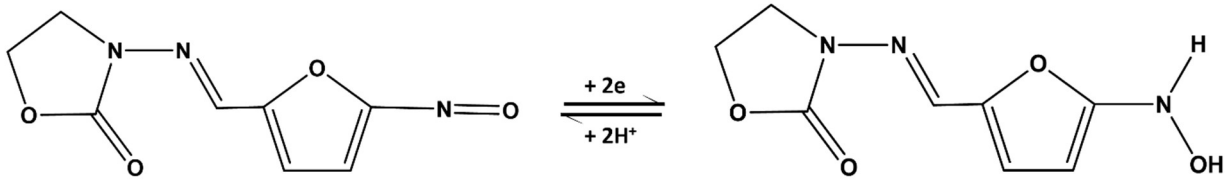

(*E*)-3-(((5-nitrosofuran-2-yl)methylene)amino)oxazolidin-2-one

Furazolidone (-NO)

(*E*)-3-(((5-(hydroxyamino)furan-2-yl)methylene)amino)oxazolidin-2-one

Furazolidone (-NHOH)

Fig 8 C. The overall reduction mechanism of the furazolidone.

3.6 Impact of different concentration on *f*-MWCNTs/SPCE

In addition, the effect of analyte concentration on *f*-MWCNTs/SPCE is been investigated by the addition of different amounts of FUR in presence of 0.05M PBS at a scan rate of 0.05 mV/s^{-1}. **Fig 9 A** which reveals the CV response at multiple concentrations of FUR on *f*-MWCNTs/SPCE, the peak current is gradually increases with increasing of concentration. A sharp and strong peak is been exposed to a shift in reduction potential. Here, the reduction peak specifies that increase in FUR from 10 to 400 micromoles the reduction peak also increase gradually where the linearity regression exhibited in (**Fig. 9 B**). Over the lateral proportionality of increase in the concentration, this endorses *f* f-MWCNTs/SPCE has good linearity with the addition of an analyte, where it is also has the good electrocatalytic activity against the FUR.

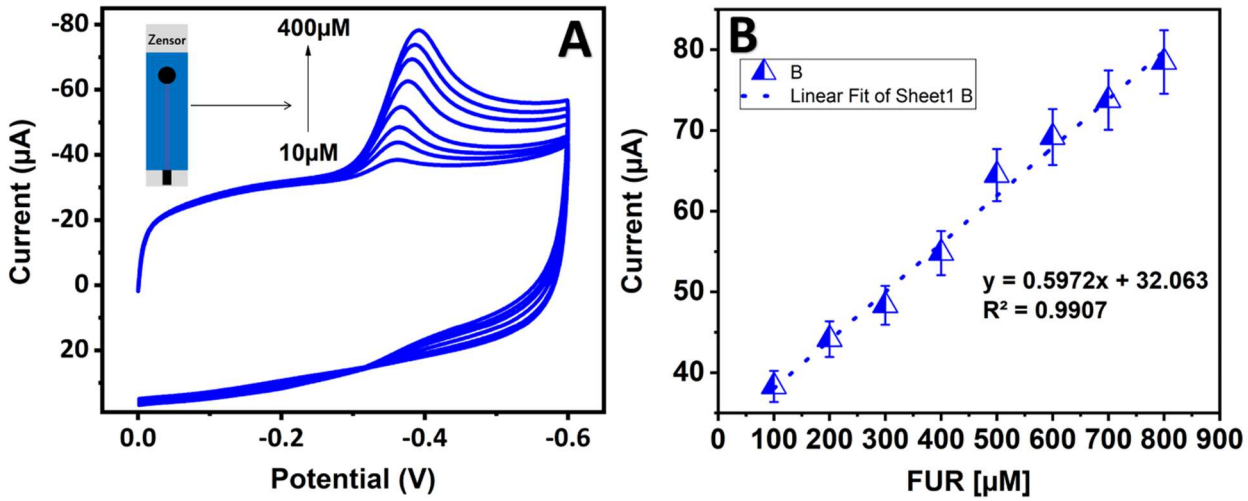

Fig 9. Different additions of FUR in the presence of 0.05M PBS on *f*-MWCNTs/SPCE and the linear plot shown in **(B).**

3.7 Influence of potential sweep rate on *f*-MWCNTs/SPCE

To further examine the electrochemical reduction mechanism of FUR, the influence of scan rate (*v*) on the voltammetry response of FUR using *f*-MWCNTs/SPCE was studied in detail. **Fig 10 (A)** shows the CV analysis of *f*-MWCNTs/SPCE in 0.05M PBS (pH-7.0) with 100µM FUR at scan rates ranging from 0.1 to 0.5 V/s^{-1}. A significant link between peak current and scan rate was discovered. The linear regression equations are illustrated in equations (6). **Figure 10 (B)** shows that the FUR reductive reaction occurs at the *f*-MWCNTs/SPCE, indicating a diffusion-controlled mechanism.

$$I_{pa}/A = y = 70.01x + 111.43 \; R^2 = 0.997 \rightarrow (6)$$

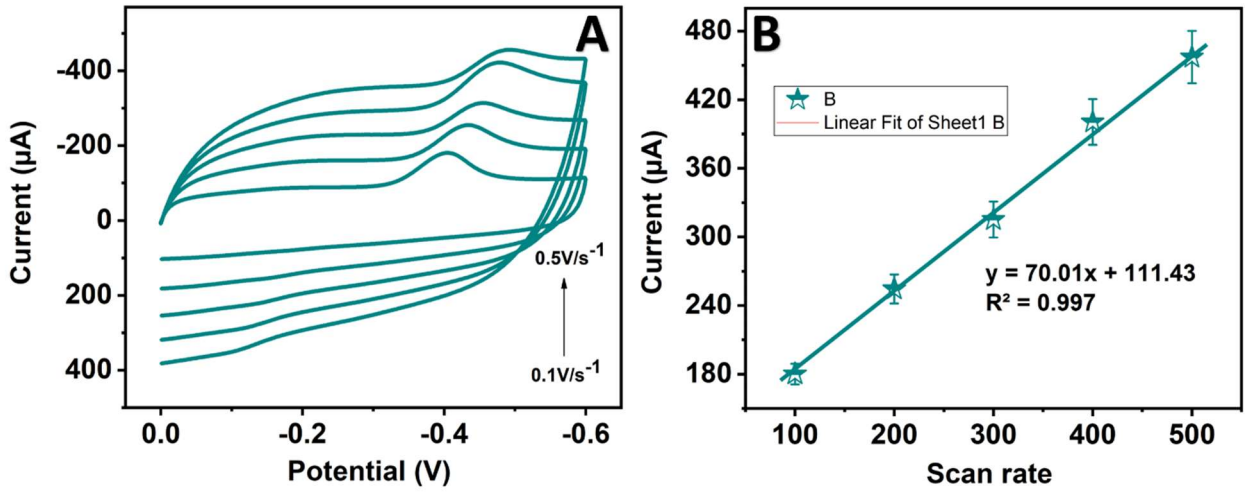

Fig 10 (A). Different scan rate for FUR on the modified electrodes and the linearity plot in **(B).**

Besides, the plots of E_p (anodic) *vs*. log υ exhibits the straight line with slopes of -2.3RT/(1-α) nF and -2.3RT/αnF for the E_{pa} **[**43**]**. Here, α and n_a (=1) are electron transfer coefficient and number of electrons involved in the rate determining step, while the constants R, T and F represents their usual meanings (R=8.314 J $Kmol^{-1}$, T=298K, F=96485C mol^{-1}). The charge transfer coefficient can be calculated from Tafel slopes. The value of α is 0.01193 (±0.015) which is close to 0.5 means that the activated complex is around halfway between reactants and products on the reaction coordinate. In the other words, structure of the activated complex reflecting reactants and products equally. Also, the relationship between scan rate current *vs.* potential can be expressed in the **Fig 11 A.** From this data plot we obtained the linear regression value of R^2=0.989.

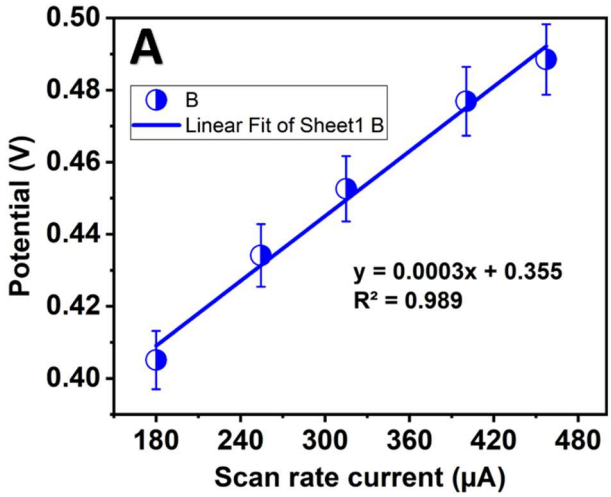

Fig 11 A. Potential *vs* scan rate current realtionship.

Figure 11 B shows Tafel graphs that demonstrate the connection between reductive potentials and the log of various scan speeds in seconds. The slope value may be used to determine the electron transfer coefficient. The activated complex is roughly halfway between the target analyte and the final product on the reaction coordinate. In other words, the structure of an active compound is equally representative of both reactants and products. Equation (7) shows the relationship between potential and the log of scan rate:

$$Ipc/A=y=0.01193x +0.1635 \; R2\text{-}0.9914 \rightarrow (7)$$

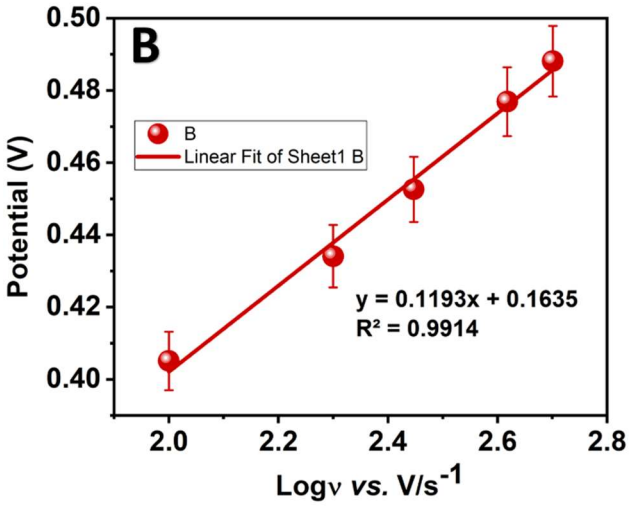

Fig 11 B. Tafel plot (log of scan rate vs Potential).

3.8 Influence of the pH

pH acts as a prominent parameter in describing the electrocatalytic nature as the target analyte FUR may have an advantage and can influence the electrocatalytic reduction by the transportation of electron and proton. To this, CV was performed for *f*-MWCNTs/SPCE in the presence of 100 µM FUR in multiple pH solutions from 3.0 to 7.0 with a constant scan rate of 0.05mV/s^{-1}. **Fig 12 A** illustrates the reduction peak of FUR current is increased with the pH from 3,4,5,6 and 7, where the cathodic peak current has achieved at pH-7.0. Here, cathodic peak current has decreased which specifies that the H^+ ions have a clear impact on the chemical reduction. Here the electro-reduction mechanism of FUR is shown in **Fig 12**. Making an allowance for sensitivity at pH-7 is selected as an appropriate electrolyte in the further electrochemical studies. And the corresponding response current visualization present in the **Fig 12 B**.

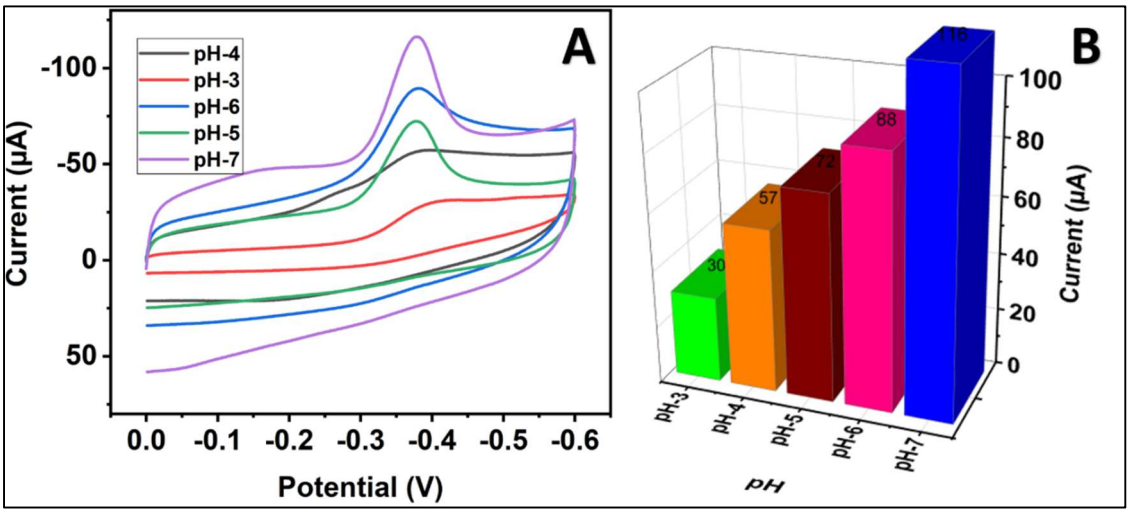

Fig 12. pH studies of FUR on *f*-MWCNTs/SPCE and obtained response current value **(B)**

3.9 practical application of FUR on *f*-CB/WC/SPC electrode

By cyclic voltammetry studies, it is confirmed that our proposed catalyst *f*-MWCNTs/SPCE electrode has a good current response, noticeable catalytic activity, large surface area and extreme fast electro transfer rate on FUR. In finding the linear response and limit of detection (LOD) of FUR towards *f*-MWCNTs/SPCE on a modified rotating disk electrode (RDE), Amperometric (i-t) current response studies were carried out. **Fig. 13 A** discloses the current variations in a step wise injection of FUR under N_2 saturated pH-7.0(PBS) and the corresponding obtained linear regression plot shown in **Fig. 13 B**. Further down in optimized environments, the i-t response is directly proportional with an increase in the concentration of FUR under the range conditions of 1nM to 1396 µM. Here the limit of detection (LOD) is found to be 1nM and the limit of quantification (LOQ) 1.16nM, thus exceeded formerly stated FUR sensors. A comparative study on analytical parameters has been done in the aspect of LOD, the linear range of response, by considering previous reported electrochemical sensors (**Table 2**) in detecting FUR. The obtained sensitivity of the developed sensor has shown 2.6485cm^2/s.

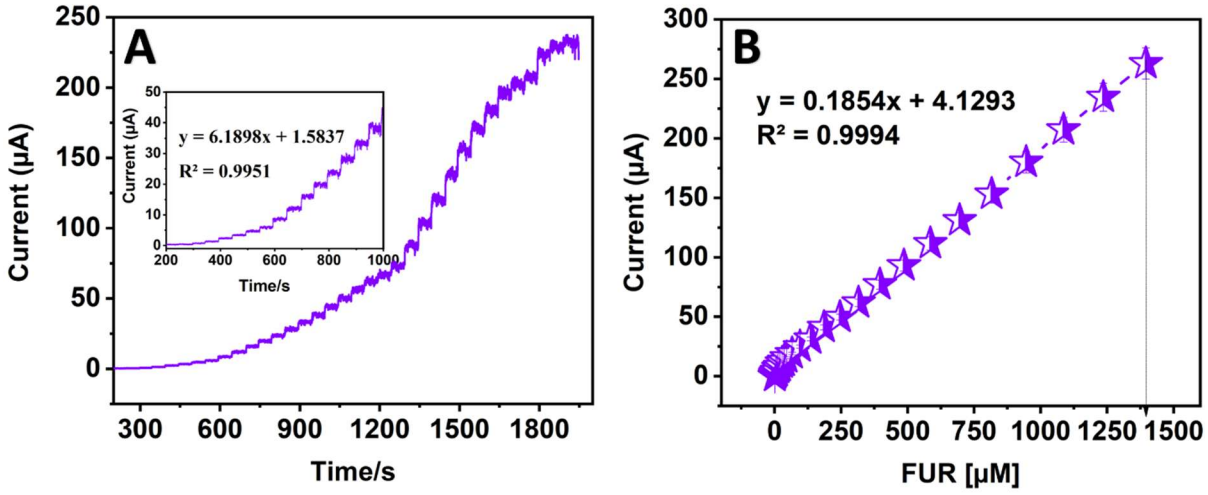

Fig 13. Amperometric response of FUR using *f*-MWCNTs/SPCE in presence of 0.05M PBS (pH-7.0) with the successive addition from lower to higher concentration.

Table 2 Comparison table for the detection of FUR with previously reported sensors.

Electrodes	Technique	Linear range (μM)	LOD (μM)	LOQ	Ref
$FeWO_4$/CB/GCE	DPV	0.01–135	0.01	Nill	31
tNP/$COF_{TFPB-DHzDS}$@rGO	DPV	15-110	0.05	Nill	32
Au-Ag-ANCCs/ZnO-NPs-CPE/PEO	SWV	0.9-360	0.023	0.076 PM	33
COF@NH_2-CNT	DPV	0.2-100	7.75	Nill	34
ZW NPs	DPV	0.1-849	13	Nill	35
Co-MOF@CB	DPV	0.4–610	0.0875	Nill	36
$MnTiO_3$	DPV	0.05-1101.6	4.05	Nill	37
CrG	DPV	0.1-88	15.6	52.03 nM	38
SnO_2/MoO_3	DPV	0.01–200	0.01	Nill	39
Bi-MOF/f-CNF	DPV, i-t	0.199-238	20.8	Nill	40
ZnO/$ZnFe_2O_4$	DPV	1–100	0.65	Nill	41
f-MWCNTs/SPCE	i-t	0.001-1396	1nM	1.16nM	This work

4.Precision, specificity, repeatability and storage stability analysis

To examine the specificity of the developed sensor was investigated in presence of some similar structure oxidizing chemicals and common ions (a-m, Table **3**) were the results are analyzed. **Fig 14** describes the i-t response of the *f*-MWCNTs/SPCE against 100 μM of FUR and 20-folds higher concentration of interfering species (above mentioned). There is no significant interference was found for the detection of FUR. These

results revealed that the electrode quickly responded to FUR and interfering substances. However, very quiet responses were observed when each interfering compounds were injected separately (without FUR). This result suggests excellent selectivity of the *f*-MWCNTs/SPCE. As a result, the constructed sensor can be used in real-time to determine FUR. Table **3** explain the reference of interfering species.

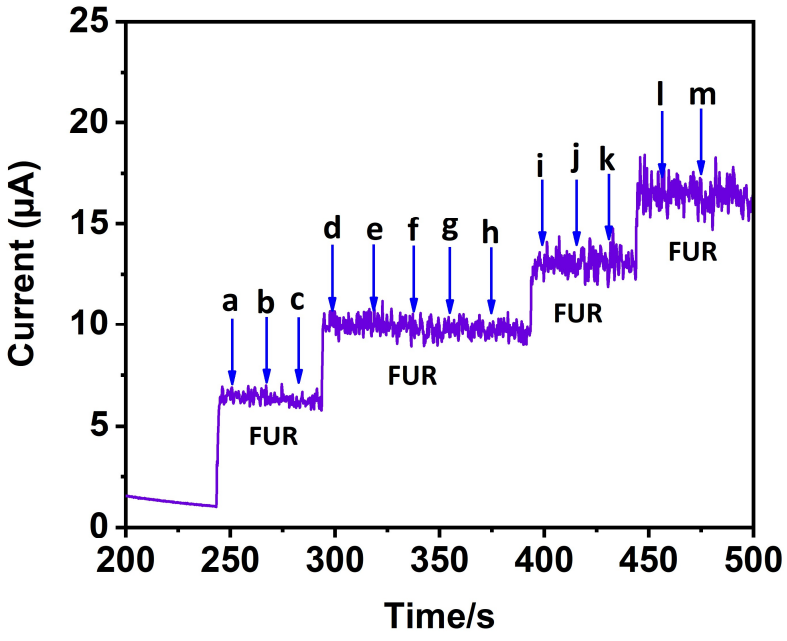

Fig 14. Selectivity studies of FUR sensor with various analytes with the addition of 100μM of target analyte (0.05M , pH-7.0).

Reference	Interference species name
a	Dimetrozolidone
b	Carbamacibine
c	Dopamine
d	Hydrogen peroxide
e	Glucose
f	Citric acid
g	Vitamin-C
h	Paracetamol
i	Pb
j	Cd
k	SO_4^-
l	Arsenic
m	Cl_2

Table 3. Interfering species.

To investigate the stability of the *f*-MWCNTs modified electrode current response of reduction peaks of FUR are calculated at different time periods. The modified electrode was kept under the room temperature

at pH-7.0 (PB solution). To the modified electrode initial current response was retained around ~99.91%, which indicates the modified electrode has good stability under a lateral cathodic current response of 100 µM FUR for 42 days **(Fig. 15 A)** with the comparison distribution current values is show in **Fig 15 B**.

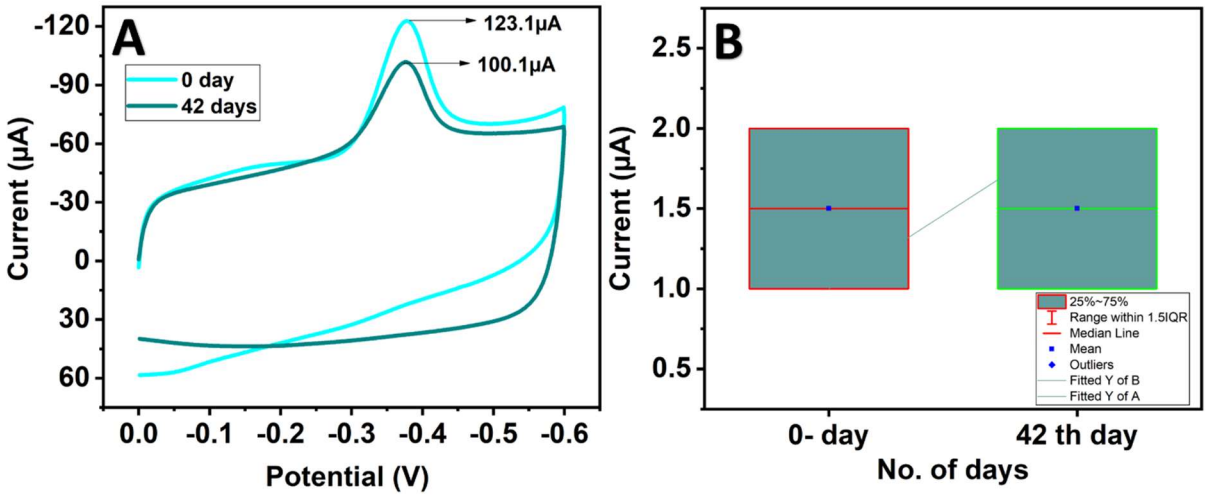

Fig 15. (A) Stability analysis of the fabricated sensor in presence of 0.05M PBS, pH-7.0 with 100 µM of an analyte and corresponding whisker plot **(B)**.

To analyze the reproducibility of the modified electrode 100 µM of FUR is measured on three different electrodes which are prepared by using analog procedure. **(Fig. 16).**

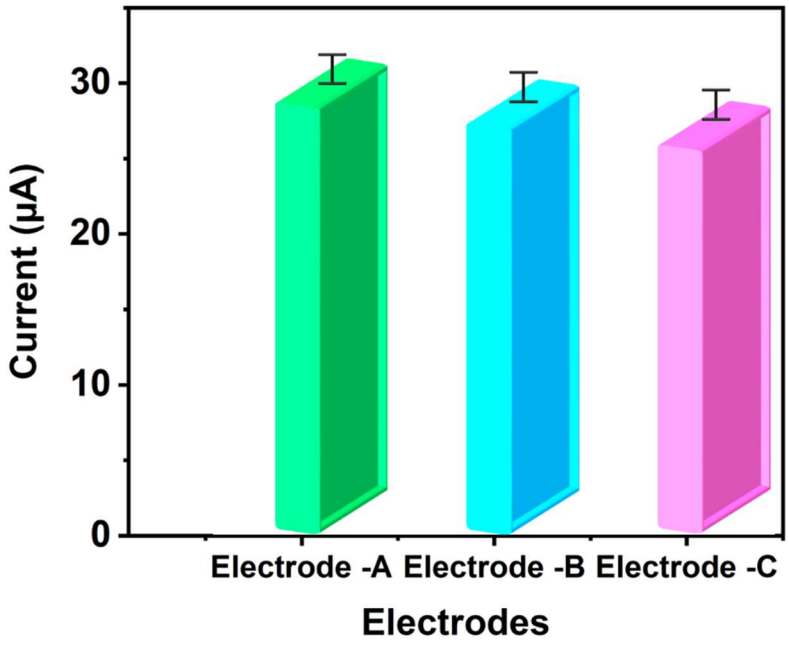

Fig 16. Reproducibility of the developed sensor.

By which it is proved that *f*-MWCNTs/SPCE electrode has a satisfactory reproducibility. Continuing, to *f*-MWCNTs/SPCE electrode repeatability analysis was done by using three sub-sequential determinations **(Fig. 17)**, which implies that the modified electrode has outstanding repeatability.

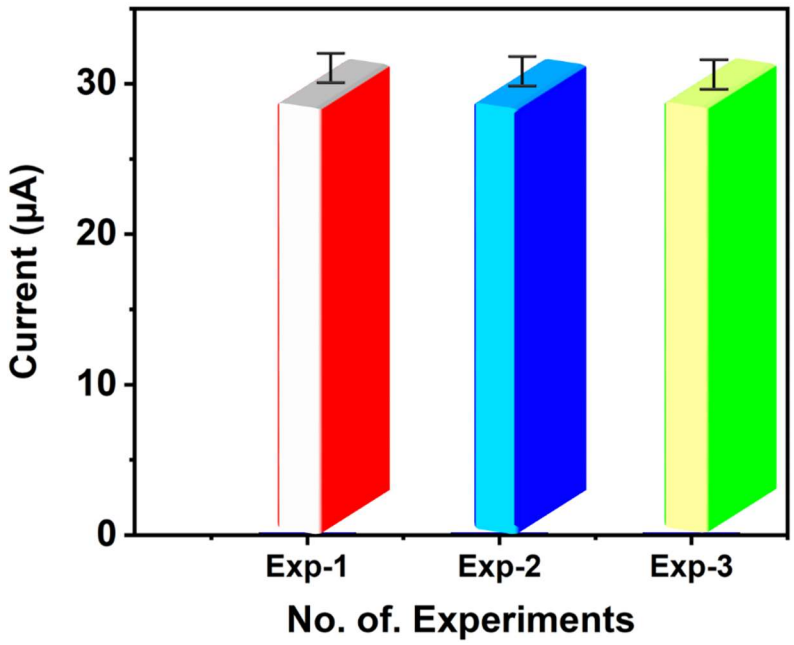

Fig 17. Repeatability of the developed sensor.

4.1 Real time application of *f*-MWCNTs/SPCE in biological samples

In order to ensure the practical applicability of the proposed sensor (FUR) were quantified in human urine (HU), artificial saliva (AS) and human serum (HS) on *f*-MWCNTs/SPCE. This sample was prepared before the experiment and three parallel determinations were carried out for this detection aforementioned biological samples and **Fig. 18**, **19,** and **20** present the database. Consequently, the results obtained demonstrate the practical applications of the constructed sensor in actual samples.

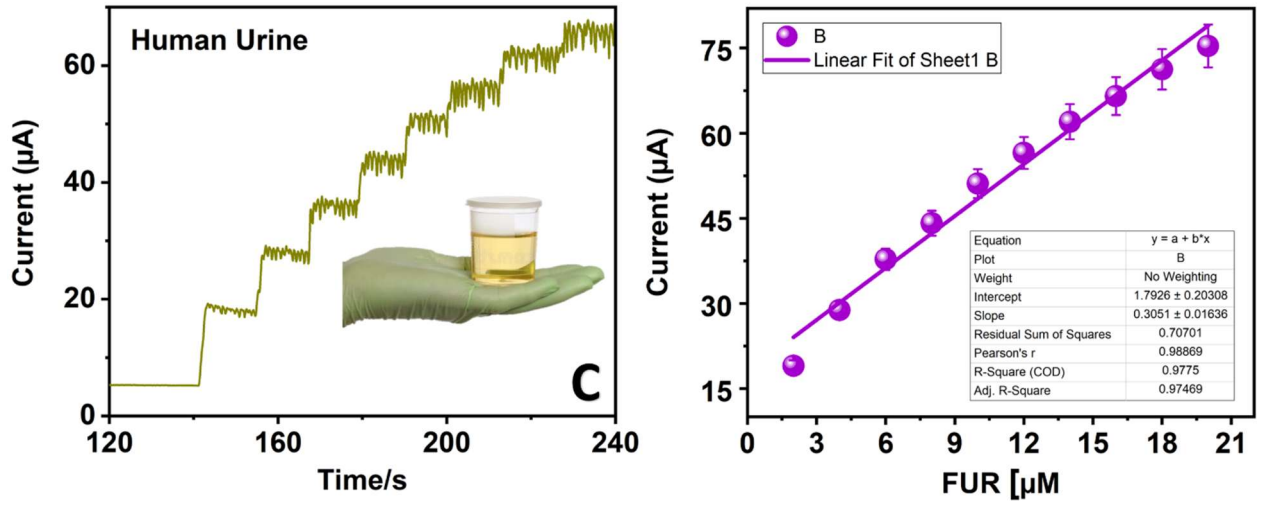

Fig 18. Real-time application in human urine sample.

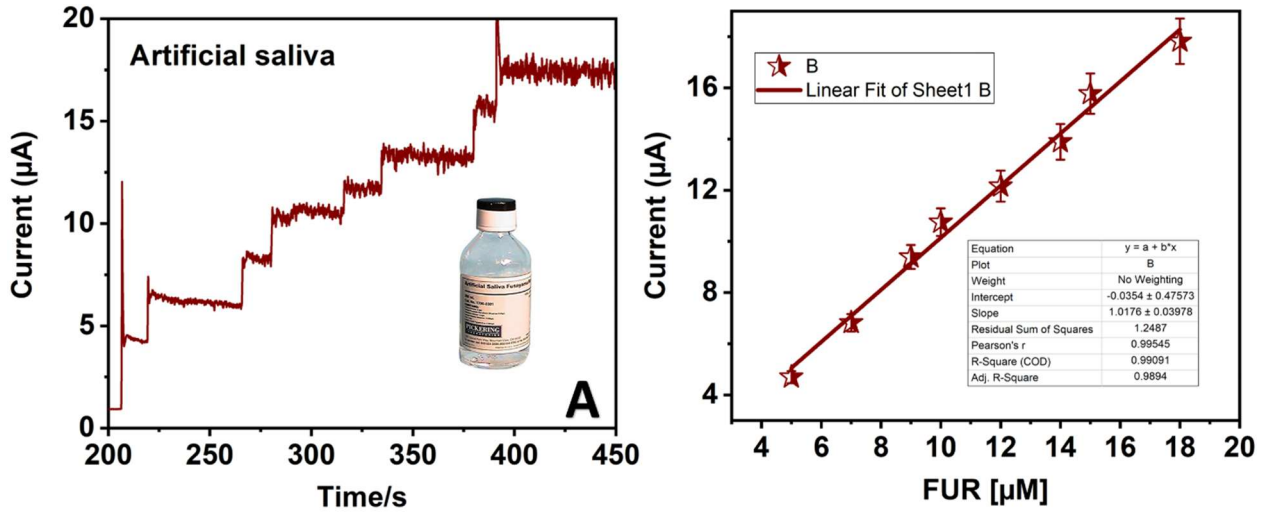

Fig 19. Real-time application in artificial saliva.

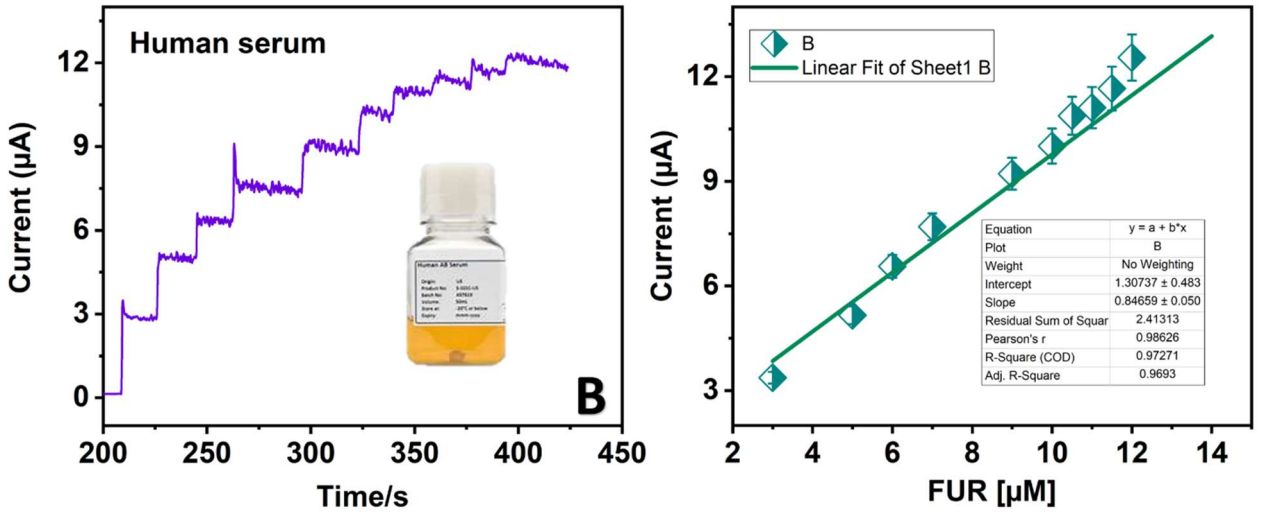

Fig 20. Real-time application in human serum sample.

Metabolic acitivity of furazolidone:

Additionally, the metabolic activity of the furazolidone in human liver is detailed **(Fig 21)**. Furazolidone is rapidly and extensively metabolized; the primary metabolic pathway identified begins with nitro-reduction to the aminofuran derivative. Two major metabolites are produced: 3-amino-2-oxazolidone (AOZ) or beta-hydroxyethylhydrazine (HEH). AOZ is responsible for monoamine oxidase inhibition. Detoxification and elimination of the drug is done primarily by conjugation with glutathione.

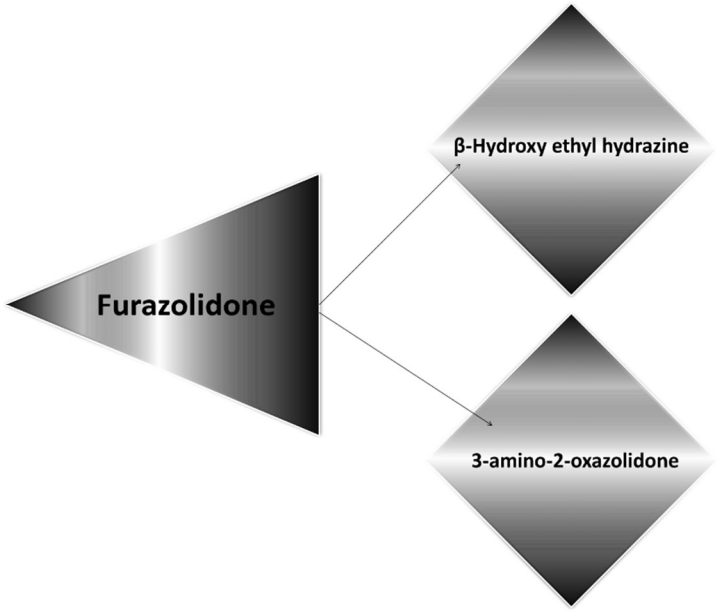

Fig 21. Metabolic acitivity of the furazolidone in human liver.

5. conclusion

Summary of the research work, we have constructed the technologically advanced electrochemical sensor for the effective selection and sensitization, to determine the furazolidone (FUR) which was constructed by green chemical synthesis method. These electrode materials' morphological characteristics were suitably and structurally described utilizing XRD, FTIR, EIS, Raman spectra, FE-SEM and HRTEM. The electrochemical property enhancement of the modified electrode toward the detection of FUR was confirmed by CV and Amperometric techniques. The experimental results suggests that the prepared electrochemical sensor showed an excellent specificity for the quantification of FUR in presence of potentially co-interfering analytes with a wide linear response range, lower limit of detection, limit of quantification and good sensitivity. Due to this excellent behaviour, the fabricated sensor can be used for the efficient determination of FUR in biological samples in future. Furthermore, the proposed synthesis method

is simple, fast, scale-up production, robust, reproducible and does not require any sophisticated instruments. In future, the present process can be further extended for the construction of various morphologies and to check their possible applications in lithium-ion batteries, fuel cells, and photocatalysis.

Reference and bibilography:

1. Meng, J., Mangat, S.S., Grudzinski, I.P. and Law, F.C.P., 1998. Evidence of 14C-furazolidone metabolite binding to the hepatic DNA of trout. Drug metabolism and drug interactions, 14(4), pp.209-220.
2. Timperio, A.M., Kuiper, H.A. and Zolla, L., 2003. Identification of a furazolidone metabolite responsible for the inhibition of amino oxidases. Xenobiotica, 33(2), pp.153-167.
3. Ali, B.H., 1999. Pharmacological, therapeutic and toxicological properties of furazolidone: some recent research. Veterinary research communications, 23(6), pp.343-360. Hoogenboom, L.A.P., Tomassini, O., Oorsprong, M.B.M. and Kuiper, H.A., 1991. Use of pig hepatocytes to study the inhibition of monoamine oxidase by furazolidone. Food and Chemical Toxicology, 29(3), pp.185-191.
4. Liu, S., Dou, L., Yao, X., Zhang, W., Zhao, B., Wang, Z., Ji, Y., Sun, J., Xu, B., Zhang, D. and Wang, J., 2020. Polydopamine nanospheres as high-affinity signal tag towards lateral flow immunoassay for sensitive furazolidone detection. Food chemistry, 315, p.126310.
5. Feitosa, I.B., Mori, B., Santos, A.P.D.A.D., Villanova, J.C.O., Teles, C.B.G. and Costa, A.G., 2021. What are the immunopharmacological effects of furazolidone? A systematic review. Immunopharmacology and Immunotoxicology, 43(6), pp.674-679.
6. Su, L., Wang, L., Yao, X., Yin, X., Zhang, H., Zhao, M., Liu, S., Wang, Z., Wang, J. and Zhang, D., 2020. Small size nanoparticles -Co3O4 based lateral flow immunoassay biosensor for highly sensitive and rapid detection of furazolidone. Talanta, 211, p.120729.
7. Sun, Y., Waterhouse, G.I., Xu, L., Qiao, X. and Xu, Z., 2020. Three-dimensional electrochemical sensor with covalent organic framework decorated carbon nanotubes signal amplification for the detection of furazolidone. Sensors and Actuators B: Chemical, 321, p.128501.
8. Liu, S., Dou, L., Yao, X., Zhang, W., Zhao, B., Wang, Z., Ji, Y., Sun, J., Xu, B., Zhang, D. and Wang, J., 2020. Polydopamine nanospheres as high-affinity signal tag towards lateral flow immunoassay for sensitive furazolidone detection. Food chemistry, 315, p.126310.
9. Su, L., Chen, Y., Wang, L., Zhang, H., Sun, J., Wang, J. and Zhang, D., 2021. Dual-signal based immunoassay for colorimetric and photothermal detection of furazolidone. Sensors and Actuators B: Chemical, 331, p.129431.

10. Baranwal, J., Barse, B., Gatto, G., Broncova, G. and Kumar, A., 2022. Electrochemical sensors and their applications: A review. Chemosensors, 10(9), p.363.
11. Xiao, Z., Elike, J., Reynolds, A., Moten, R. and Zhao, X., 2016. The fabrication of carbon nanotube electronic circuits with dielectrophoresis. Microelectronic Engineering, 164, pp.123-127.
12. Sun, L., Wang, X., Wang, Y. and Zhang, Q., 2017. Roles of carbon nanotubes in novel energy storage devices. Carbon, 122, pp.462-474.
13. Oliveira, T.M. and Morais, S., 2018. New generation of electrochemical sensors based on multi-walled carbon nanotubes. Applied Sciences, 8(10), p.1925.
14. Liu, L., Niu, Z. and Chen, J., 2018. Flexible supercapacitors based on carbon nanotubes. Chinese Chemical Letters, 29(4), pp.571-581.
15. Parveen, S., Kumar, A., Husain, S. and Husain, M., 2017. Fowler Nordheim theory of carbon nanotube based field emitters. Physica B: Condensed Matter, 505, pp.1-8.
16. Sudha, P.N., Sangeetha, K., Vijayalakshmi, K. and Barhoum, A., 2018. Nanomaterials history, classification, unique properties, production and market. In Emerging applications of nanoparticles and architecture nanostructures (pp. 341-384). Elsevier.
17. Soriano, M.L., Zougagh, M., Valcárcel, M. and Ríos, Á., 2018. Analytical Nanoscience and Nanotechnology: Where we are and where we are heading. Talanta, 177, pp.104-121.
18. Adams, F.C. and Barbante, C., 2013. Nanoscience, nanotechnology and spectrometry. Spectrochimica Acta Part B: Atomic Spectroscopy, 86, pp.3-13.
19. Zaporotskova, I.V.; Boroznina, N.P.; Parkhomenko, Y.N.; Kozhitov, L.V. Carbon nanotubes: Sensor properties. A review. Mod. Electron. Mater. 2016, 2, 95–105.
20. Dumitrescu, I.; Unwin, P.R.; Macpherson, J.V. Electrochemistry at carbon nanotubes: Perspective and issues. Chem. Commun. 2009, 6886–6901.
21. Hamada, N., Sawada, S.I. and Oshiyama, A., 1992. New one-dimensional conductors: Graphitic microtubules. Physical review letters, 68(10), p.1579.
22. Mao, J.; Wang, Y.; Zhu, J.; Yu, J.; Hu, Z. Thiol functionalized carbon nanotubes: Synthesis by sulfur chemistry and their multi-purpose applications. Appl. Surf. Sci. 2018, 447, 235–243.
23. Sinnott, S.B. and Andrews, R., 2001. Carbon nanotubes: synthesis, properties, and applications. Critical reviews in solid state and materials sciences, 26(3), pp.145-249.
24. Fonseca, A. and Nagy, J.B., 2001. Carbon nanotubes formation in the arc discharge process. In Carbon Filaments and Nanotubes: Common Origins, Differing Applications? (pp. 75-84). Dordrecht: Springer Netherlands.

25. Journet, C., Maser, W.K., Bernier, P., Loiseau, A., de La Chapelle, M.L., Lefrant, D.S., Deniard, P., Lee, R. and Fischer, J.E., 1997. Large-scale production of single-walled carbon nanotubes by the electric-arc technique. nature, 388(6644), pp.756-758.
26. Guo, T., Nikolaev, P., Rinzler, A.G., Tomanek, D., Colbert, D.T. and Smalley, R.E., 1995. Self-assembly of tubular fullerenes. The Journal of Physical Chemistry, 99(27), pp.10694-10697.
27. Manafi, S., Rahaei, M.B., Elli, Y. and Joughehdoust, S., 2010. High-yield synthesis of multi-walled carbon nanotube by hydrothermal method. The Canadian Journal of Chemical Engineering, 88(2), pp.283-286.
28. Hsu, W.K., Hare, J.P., Terrones, M., Kroto, H.W., Walton, D.R.M. and Harris, P.J.F., 1995. Condensed-phase nanotubes. Nature, 377(6551), pp.687-687.
29. Laplaze, D., Bernier, P., Maser, W.K., Flamant, G., Guillard, T. and Loiseau, A., 1998. Carbon nanotubes: the solar approach. Carbon, 36(5-6), pp.685-688.
30. David, M.E., Ion, R.M., Grigorescu, R.M., Iancu, L., Andrei, E.R., Somoghi, R., Frone, A.N. and Stirbescu, R.M., 2020, November. Chemical Synthesis of Multi-Walled Carbon Nanotubes and Their Functionalization with Carboxylated Groups. In Proceedings (Vol. 57, No. 1, p. 45). MDPI.
31. Sivaji, S.P., Mariappan, K., Chen, T.W., Chen, S.M., Alagarsamy, S., Sakthinathan, S., Chiu, T.W., Al-Mohaimeed, A.M., Ali, M.A. and Elshikh, M.S., 2024. Effective electrochemical detection of furazolidone based on iron tungstate decorated carbon black composite modified glassy carbon electrode. Colloids and Surfaces A: Physicochemical and Engineering Aspects, 697, p.134361.
32. Chen, R., Peng, X., Song, Y. and Du, Y., 2022. A Paper-Based Electrochemical Sensor Based on PtNP/COFTFPB-DHzDS@rGO for Sensitive Detection of Furazolidone. Biosensors, 12(10), p.904.
33. Adane, W.D., Chandravanshi, B.S. and Tessema, M., 2024. A pioneering electrochemical sensor for the simultaneous determination of nitrofurantoin and furazolidone residues in food and municipal wastewater samples. Sensing and Bio-Sensing Research, 45, p.100678.
34. Sun, Y., Waterhouse, G.I., Xu, L., Qiao, X. and Xu, Z., 2020. Three-dimensional electrochemical sensor with covalent organic framework decorated carbon nanotubes signal amplification for the detection of furazolidone. Sensors and Actuators B: Chemical, 321, p.128501.
35. Rajakumaran, R., Krishnapandi, A., Chen, S.M., Balamurugan, K., Chang, F.M. and Sakthinathan, S., 2021. Electrochemical investigation of zinc tungstate nanoparticles; a robust sensor platform for the selective detection of furazolidone in biological samples. Microchemical Journal, 160, p.105750.

36. Selvam, A., Gopika, M.G., Kuo, C.Y., Saraswathyamma, B., Yusuf, K. and Govindasamy, M., 2025. Co-MOF-67/carbon black composite: A novel electrochemical platform for furazolidone detection for food analysis. Food Chemistry, p.145023.
37. Amalraj, A.J.J. and Wang, S.F., 2022. Synthesis of transition metal titanium oxide (MTiOx, M=Mn, Fe, Cu) and its application in furazolidone electrochemical sensor. Journal of Industrial and Engineering Chemistry, 111, pp.356-368.
38. Govindharaj, A., Munaf, M., Chen, S.M., Tamilalagan, E. and Renganathan, V., 2025. Hydrothermally anchored copper oxides nanoflakes on reduced graphene oxide for Furazolidone electrochemical detection. Microchemical Journal, 215, p.114266.
39. Pandi Sivaji, S., Chen, S.M., Lee, D. and Muthukutty, B., 2025. High-performance electrochemical detection of furazolidone: Investigating the synergistic effects of SnO2/MoO3 and carbon black composite.
40. Varatharajan, P., Rajaji, U., Rani, S.K., Vasimalai, N. and Govindasamy, M., 2024. Ultrasonic synthesis of MOF-based hybrid composite for electrochemical detection of furazolidone antibiotic in food and biological samples. Surfaces and Interfaces, 55, p.105384.
41. Anh, N.T., Huyen, N.N., Dinh, N.X., Vinh, L.K., Tung, L.M., Vinh, N.T., Van Quy, N., Lam, V.D. and Le, A.T., 2022. ZnO/ZnFe 2 O 4 nanocomposite-based electrochemical nanosensors for the detection of furazolidone in pork and shrimp samples: exploring the role of crystallinity, phase ratio, and heterojunction formation. New Journal of Chemistry, 46(15), pp.7090-7102.
42. M.A. Ansari, and N. Jahan, 2021. Structural and optical properties of BaO nanoparticles synthesized by facile Co-precipitation method. Materials Highlights, 2(1), pp.23-28.
43. E. Laviron, 1979. General expression of the linear potential sweep voltammogram in the case of diffusionless electrochemical systems. J.Electroanal. Chem 101 (1979) 19-28.
44. Jia, Q., Venton, B. J., & DuBay, K. H. (2022). Structure and Dynamics of Adsorbed Dopamine on Solvated Carbon Nanotubes and in a CNT Groove. *Molecules*, *27*(12), 3768. https://doi.org/10.3390/molecules 27123768.